



# Springback prediction and validation in hot forming of a double-curved component in alloy 718

Lluís Pérez Caro<sup>1,2</sup> · Eva-Lis Odenberger<sup>1,2</sup> · Mikael Schill<sup>3</sup> · Fredrik Niklasson<sup>4</sup> · Pia Åkerfeldt<sup>5</sup> · Mats Oldenburg<sup>2</sup>

Received: 22 October 2019 / Accepted: 18 January 2021 / Published online: 8 February 2021  
© The Author(s) 2021

## Abstract

The demands associated with the production of advanced parts made of nickel-base superalloys are continuously increasing to meet the requirements of current environmental laws. The use of lightweight components in load-carrying aero-engine structures has the potential to significantly reduce fuel consumption and greenhouse gas emissions. Furthermore, the competitiveness of the aero-engine industry can benefit from reduced production costs and shorter development times while minimizing costly try-outs and increasing the efficiency of engines. The manufacturing process of aero-engine parts in superalloys at temperatures close to 950 °C produces reduced stamping force, residual stresses, and springback compared to traditional forming procedures occurring at room temperature. In this work, a hot forming procedure of a double-curved component in alloy 718 is studied. The mechanical properties of the material are determined between 20 and 1000 °C. The presence and nature of serrations in the stress–strain curves are assessed. The novel version of the anisotropic Barlat Yld2000-2D material model, which allows the input of thermo-mechanical data, is used in LS-DYNA to model the behaviour of the material at high temperatures. The effect of considering the stress-relaxation data on the predicted shape distortions is evaluated. The results show the importance of considering the thermo-mechanical anisotropic properties and stress-relaxation behaviour of the material to predict the final geometry of the component with high accuracy. The implementation of advanced material models in the finite element (FE) analyses, along with precise process conditions, is vital to produce lightweight components in advanced materials of interest to the aerospace industry.

**Keywords** Hot forming · Alloy 718 · Stress relaxation · Anisotropy · High temperature

## Introduction

The current role of the aviation industry in the reduction of carbon dioxide (CO<sub>2</sub>) emissions has been intensified to meet the requirements of increasingly stringent environmental legislations. The reduction of the thickness, and consequently,

the weight of load-carrying structures, has the potential to significantly reduce fuel consumption and improve the efficiency of engines. Traditional cold forming procedures of advanced parts made of nickel-base superalloys present some challenges, such as considerable material consumption, high amount of residual stresses and springback, high stamping

✉ Lluís Pérez Caro  
lluis.perez.caro@ri.se

Eva-Lis Odenberger  
eva-lis.odenberger@ri.se

Mikael Schill  
mikael.schill@dynamore.se

Fredrik Niklasson  
fredrik.niklasson@gknaerospace.com

Pia Åkerfeldt  
pia.akerfeldt@ltu.se

Mats Oldenburg  
mats.oldenburg@ltu.se

<sup>1</sup> Division of Materials and Production, RISE IVF AB, Vällaregatan 30, SE-293 38 Olofström, Sweden

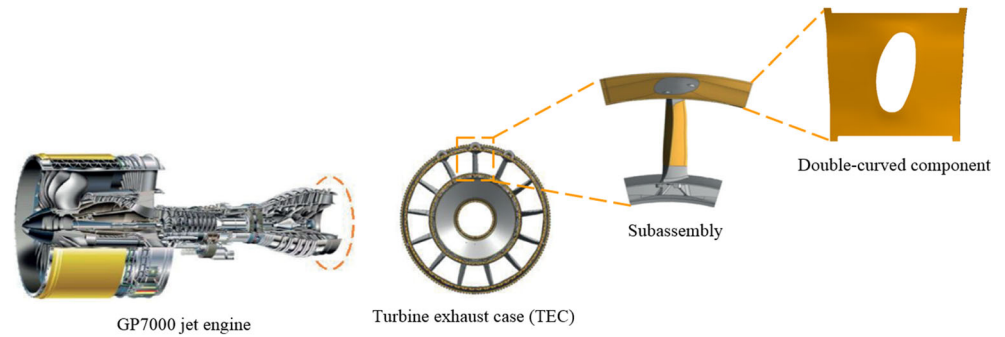
<sup>2</sup> Division of Mechanics of Solid Materials, Luleå University of Technology, SE-971 87 Luleå, Sweden

<sup>3</sup> DYNAmore Nordic AB, Brigadgatan 5, SE-587 58 Linköping, Sweden

<sup>4</sup> GKN Aerospace Engine Systems Sweden, SE-461 38 Trollhättan, Sweden

<sup>5</sup> Division of Materials Science, Luleå University of Technology, SE-971 87 Luleå, Sweden

**Fig. 1** Location of the double-curved component in a jet engine (courtesy of GKN Aerospace Sweden)



loads, and limited formability. In the manufacturing process of a turbine exhaust case (TEC), a double-curved component made of alloy 718 is welded together with other parts to form a subassembly, as illustrated in Fig. 1. Excessive shape distortions and residual stresses in the formed part may significantly affect the subsequent steps in the manufacturing chain. The economic consequences of repetitive and time-consuming try-out compensation loops can be detrimental to the competitiveness of the industry.

To overcome such difficulties, the manufacturing of complex parts in nickel-base superalloys employs advanced thermo-mechanical forming techniques, where the material is heated up to temperatures around 950 °C. Hot forming has, in general, several advantages compared to cold forming, i.e. reduced material consumption, stamping force, amount of residual stresses, and springback [1]. Some disadvantages are related to, for instance, high-energy consumption during forming and the requirement of more intermediate steps in the manufacturing chain, which, in turn, generates additional maintenance of the tool parts and thereby increases the

product cost. In addition, forming of nickel-base superalloys at intermediate temperatures may promote the precipitation of secondary phases in the matrix and, thereby, trigger the occurrence of the serrated yielding phenomenon. The formability of the blank can negatively be affected due to the inhomogeneous deformation and flow limitation of the material. Conducting the hot forming procedure at forming temperatures near 950 °C prevents precipitation hardening, while the component can be held for a specific period of time to reduce the residual stresses over the part, allowing the material to stress relax with time, thereby reducing the amount of springback. The degree of stress reduction that can be obtained in a hot forming procedure originates from the thermo-mechanical properties of the material and depends on several factors, i.e. initial stress level, temperature, and holding time [2, 3]. The process parameters, along with the anisotropy and temperature dependence of the material are vital to obtaining accurate FE predictions of the hot forming process [3–7]. Short manufacturing and delivery times can improve the competitiveness of the aviation industry. Relatively high forming

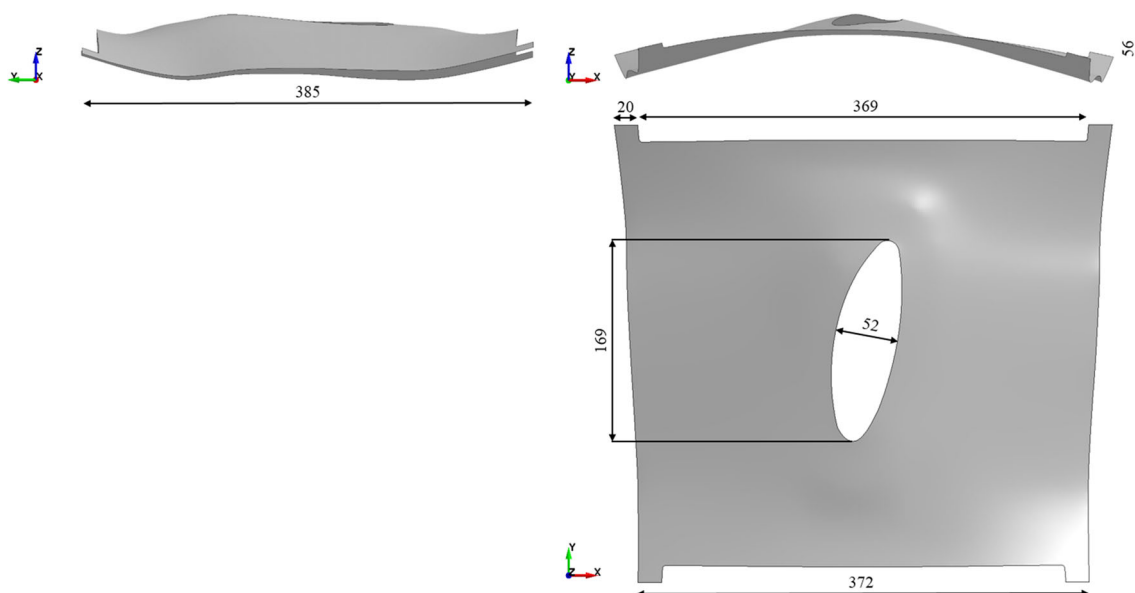


**Fig. 2** Dimensions of the double-curved component [mm]

temperatures may reduce the manufacturing time of a component while minimizing the amount of springback and residual stresses in the subsequent step in the manufacturing chain. The aim is to produce lightweight components where the final geometry of the part is secured while maintaining the required structural performance. The use of virtual shape distortion prediction and compensation tools is, therefore, key to the industry.

Several numerical studies have been performed on the springback prediction during hot forming of different materials, such as ultra-high-strength steels [1, 8, 9] and aluminum [10–13] alloys. Odenberger et al. [14] developed a hot forming procedure of a component made of Ti-6Al-4 V using FE analyses. In further work by Odenberger et al. [3, 5], they concluded that anisotropic time- and temperature-dependent material data were key to obtaining an accurate magnitude and distribution of the predicted shape deviation within the sheet thickness. Jeong et al. [15] studied the formability of Inconel 625 between 900 and 1200 °C. No previous work in the prediction of shape deviations during hot forming in alloy 718 was found in literature.

In this work, the thermomechanical manufacturing process of a double-curved component made of alloy 718 is studied, see Fig. 2. The FE analyses of the chosen hot forming procedure consist of a crash forming step at a target temperature of 950 °C, followed by stress relaxation and springback, using LS-DYNA. The mechanical properties of the material are determined between 20 and 1000 °C and used as input to the novel thermo-mechanical version of the Barlat Yld2000-2D material model based on previous work by Barlat et al. [16]. In this work, the influence of using an isotropic yield criterion in the predicted amount of springback in a hot forming simulation has been assumed a similar behaviour as previously reported by Odenberger et al. [3, 5] and Pérez Caro et al. [17]. A qualitative analysis of the shape of the stress–strain curves at high temperatures is performed. The microstructure of selected specimens is connected to the behaviour of the material at specific temperatures. A validation hot forming test is performed at approximately 900 °C to compare the predicted with the measured final shapes of the component via three-dimensional (3D) scanning and best-fit computer-aided design (CAD) evaluation. The effect of using stress relaxation data on the predicted springback of the component is assessed.

## Material

The material used in this work is the precipitation-hardenable nickel–chromium alloy 718 (UNS N07718) in the form of thin sheets with a thickness of 2.6 mm, and under the solution-annealed condition in accordance with the SAE AMS5596 specification. The chemical composition can be found in the work by Pérez Caro et al. [17].

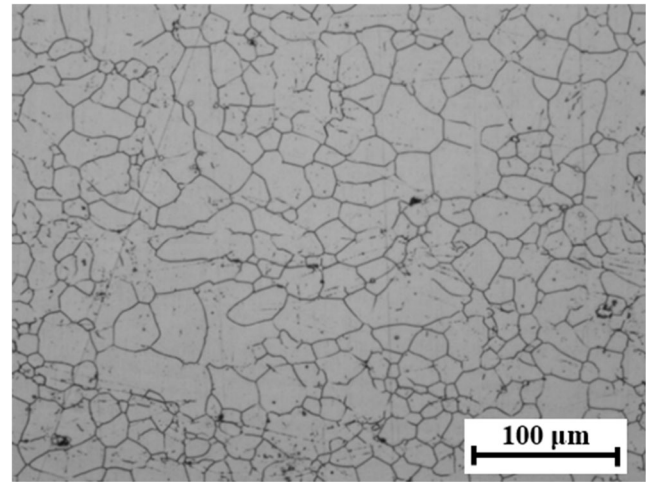


**Fig. 3** Microstructure of the specific batch of alloy 718 in the as-received condition

Figure 3 shows the typical microstructure of alloy 718 under the solution-annealed condition. The microstructure consists of the face-centred cubic (FCC)  $\gamma$ -phase matrix and sparse primary carbides, such as NbC, TiC, and  $\delta$  phase located at the grain boundaries. Alloy 718 is usually strengthened by precipitation hardening of ordered FCC  $\gamma'$ -Ni<sub>3</sub>(Al, Ti), particularly ordered body-centred tetragonal (BCT)  $\gamma''$ -Ni<sub>3</sub>Nb phases, during the subsequent aging heat treatment. Extended exposure of those precipitates to high temperatures may transform them into the detrimental  $\eta$ -Ni<sub>3</sub>Ti and  $\delta$ -Ni<sub>3</sub>Nb phases, respectively [18]. As specified in the material certificate, the material was free of Laves phase.

## Dynamic strain aging

The serrated yielding phenomenon exhibits discontinuities, such as serrations or load drops, in the stress–strain curves obtained by uniaxial tensile tests at a constant strain rate [19]. This process is also known as the Portevin-Le

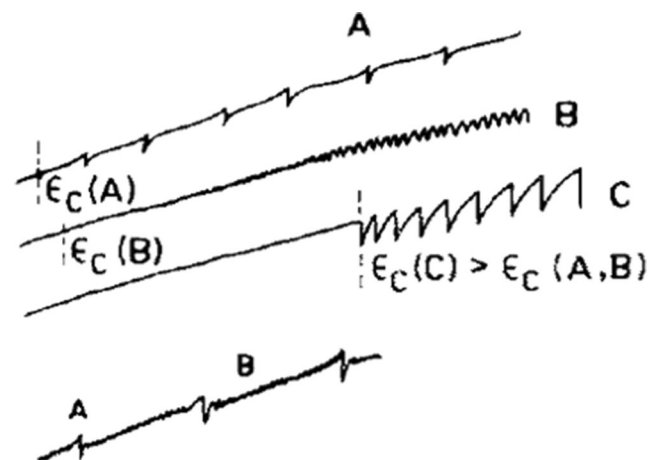
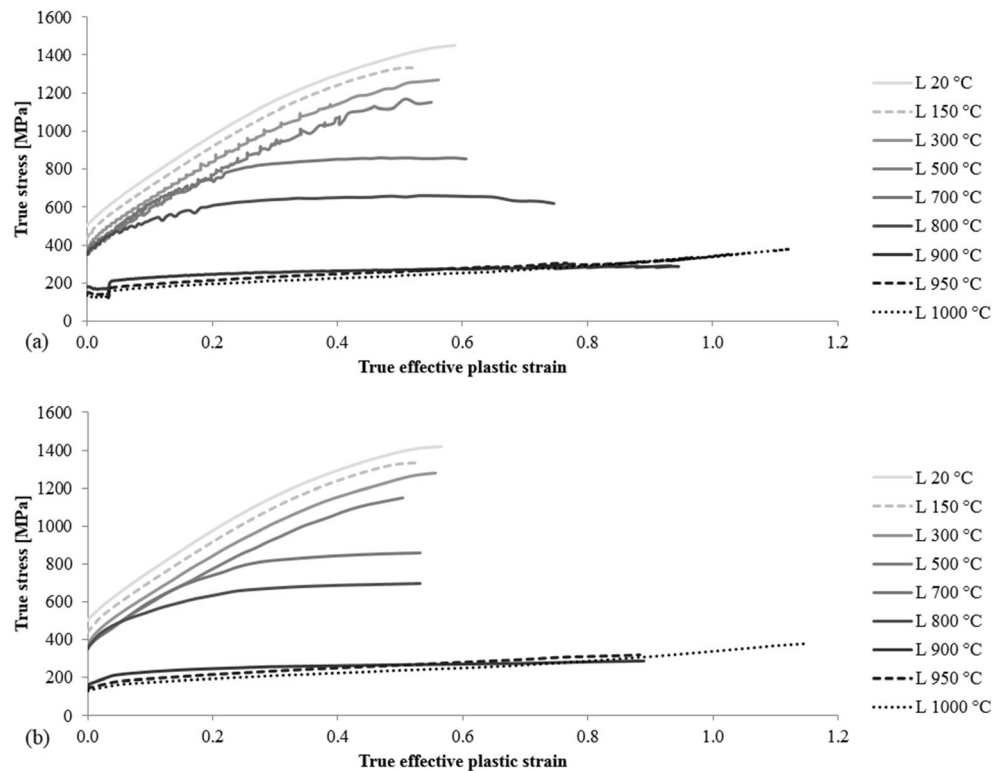


**Fig. 4** A-, B-, and C-type serrations, extracted from [19]

**Fig. 5** **a** Original and **b** smoothed flow curves for alloy 718 between 20 and 1000 °C in the L direction [31]. The hardening curve at 800 °C is added in this study for a better understanding of the behaviour of the material at elevated temperatures



Chatelier (PLC) effect [20, 21], which exhibits as a set of bands propagating across the specimen. The dynamic strain aging (DSA) effect is considered, in this study, as the physical process that causes the serrated plastic flow. The serrations are induced by the interactions between mobile dislocations and interstitial or substitutional solutes [22].

The serrations in the stress–strain curve due to DSA are usually classified into five different categories: A, B, C, D, and E, depending on both the temperature and strain rate [19]. In the A-type serrations, the stress increases and decreases above and below the mean level of the flow curve, respectively, in a periodic manner. Repeated deformation bands are

believed to initiate at the same end of the specimen and propagate in the same direction along the gauge length. They occur at relatively low temperatures and high strain rates. The B-type serrations are quick fluctuations at approximately the mean level of the hardening curve. They usually develop from the A-type serrations at relatively high strain values; however, they may also appear at the onset of serrations at higher temperatures and lower strain rates compared to those of the A-type. The increment of the stresses above the general level of the curve indicates that both A- and B-type can be considered as locking serrations. The C-type serrations appear as stress drops below the mean level of the hardening curve, indicating

**Table 1** Experimental parameters for alloy 718 between 20 and 1000 °C used to calibrate the novel version of the Barlat Yld2000-2D material model. The data at 20 °C, as well as the E-moduli, are extracted from Pérez Caro [31]. The yield stresses and Lankford coefficients are expressed in the L, D, and T directions, and in the biaxial (B) stress state

Temperature [°C]	E [MPa]	Yield stress [MPa]				Lankford coefficient		
		L	D	T	B	L	D	T
20	196,220	502.43	489.87	480.56	538.00	0.761	0.912	0.960
150	189,980	436.46	426.38	426.21	467.36	0.753	0.825	0.868
300	181,910	376.12	373.63	376.62	402.74	0.759	0.860	0.889
500	171,150	355.68	357.12	355.84	380.87	0.825	0.924	0.955
700	160,390	359.40	354.26	354.50	384.84	0.831	0.961	0.943
800	151,935	352.99	334.55	340.45	377.98	0.799	0.913	0.929
900	142,716	149.41	135.03	146.92	159.99	0.879	1.002	0.999
950	138,633	133.59	125.10	137.62	143.04	0.893	1.008	1.002
1000	134,495	131.52	100.61	105.17	140.83	0.892	1.037	1.041

**Table 2** Variation of the Young's modulus for alloy 718 as a function of temperature and strain ( $\epsilon$ ). The specimen at 800 °C fractured at approximately 15% strain

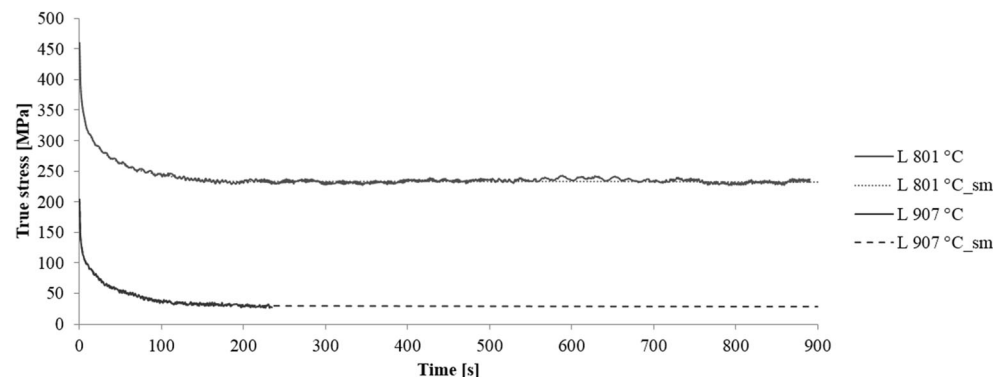
Temperature [°C]	E [MPa]			
	$\epsilon = 3\%$	$\epsilon = 8\%$	$\epsilon = 11\%$	$\epsilon = 19\%$
20	163,720	143,655	136,313	114,477
150	161,479	142,154	134,590	118,733
300	156,878	139,733	132,396	120,683
500	159,475	144,800	137,373	120,244
700	152,045	136,600	130,601	114,874
800	146,602	130,203	124,755	–
900	140,036	124,011	120,376	104,310
950	136,864	121,957	117,946	104,329
1000	132,890	119,045	115,746	106,638

that dislocations are being unlocked. They usually arise at higher temperatures and lower strain rates than those of the A- and B-type. Figure 4 illustrates the different types of serrations. Since the D- and E-type serrations are not commonly reported, they are not considered in this study.

The DSA effect has previously been studied in many nickel-base superalloys, such as alloy 718, because it occurs at the same temperature range as their typical service temperature, which may affect the properties and service life of the component. The serrated flow that occurs during the DSA phenomenon results in inhomogeneous deformation of the material, leading to negative strain rate sensitivity and, therefore, causes material instability and flow limitation during the forming process at intermediate temperatures [23]. Nalawade et al. [24] studied the presence and nature of serrations, depending on the temperature and initial microstructure, in a solution-treated alloy 718. They performed uniaxial tensile tests at a strain rate of  $6.5 \times 10^{-5} \text{ s}^{-1}$  between 200 and 700 °C. A-type serrations appeared at 200 °C, whereas B-type serrations were present between 300 and 450 °C. The latter temperature was identified as the point from where the

C-type serrations were dominant up to 700 °C. These results were validated by Hayes [25], who identified analogous types of serrations in the same temperature range. Further work by Nalawade et al. [26] included the effect of the strain rate in the serrated yielding behaviour of alloy 718. The uniaxial tensile tests at  $6.5 \times 10^{-3} \text{ s}^{-1}$  yielded no serrations at 200 °C. A-type serrations appeared at 300 °C, whereas B- or A + B-type serrations were present between 400 and 600 °C. C-type serrations were found at 650 °C. No serrations appeared at 700 °C. Similarly, the findings from Weaver and Hale [22] in a process-annealed alloy 718 at  $1.4 \times 10^{-3} \text{ s}^{-1}$  showed A- and B-type serrations in a temperature range of 231–465 °C. C-type serrations appeared between 520 and 760 °C. The same tendencies were observed by Rezende et al. [27] in a solution-annealed alloy 718 under secondary vacuum. Uniaxial tensile tests between 200 and 800 °C at a strain rate of  $3.2 \times 10^{-4} \text{ s}^{-1}$  yielded A- and B-type serrations from 200 to 450 °C, whereas C-type serrations were observed from 450 to 750 °C. No serrations were observed at 800 °C. Maj et al. [28] used statistical methods to analyse the different types of serrations present in a solution-strengthened alloy 718 subjected to uniaxial tensile testing at different temperatures and strain rates. The tensile tests performed at a strain rate of  $2 \times 10^{-3} \text{ s}^{-1}$  produced A-type serrations at 250 °C, whereas B-type serrations appeared at 300 °C. C-type serrations were present between 300 and 750 °C, with a combination of C- and A-type serrations at 600 °C.

According to Rezende et al. [27], the behaviour of solution-annealed alloy 718 at elevated temperatures can be defined by two other mechanisms apart from DSA, i.e. precipitation hardening and oxygen assisted intergranular cracking (OAIC). The OAIC phenomenon occurs due to the brittle intergranular cracking that occurs when the alloy is deformed at elevated temperatures because of oxygen penetration into the grain boundaries in the form of NbO [29, 30]. The transition from the normal to inverse behaviour of the critical strain for the onset of serrations at 600 °C indicates the beginning of simultaneous precipitation hardening and OAIC. The concentration of Nb is drastically reduced owing to the formation of  $\gamma'$  and  $\gamma''$  precipitates.

**Fig. 6** Original and smoothed (\_sm) stress relaxation curves for alloy 718 at different temperatures



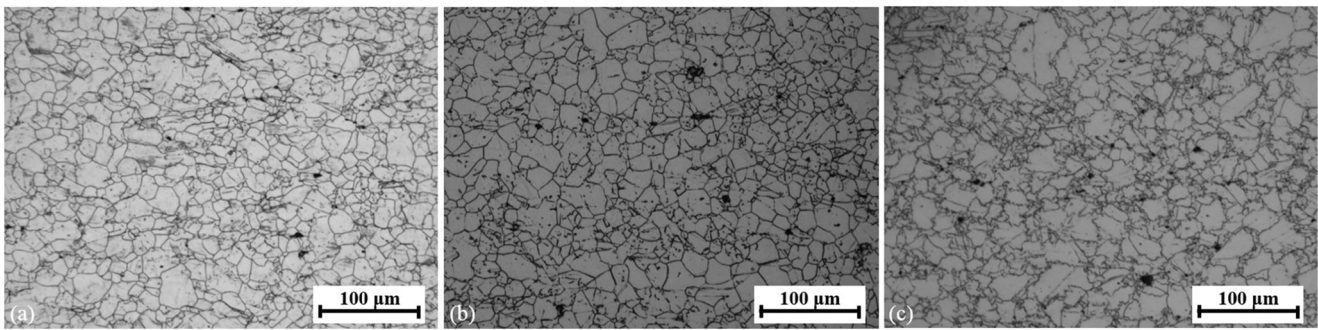


**Fig. 7** Microstructure of the specific batch of alloy 718 at (a) 20 °C, (b) 700 °C, and (c) 1000 °C

## Experimental work

### Material-characterization tests

Uniaxial tensile tests were carried out using an MTS 810 100 kN servo-hydraulic machine and the digital image correlation (DIC) system ARAMIS™ for strain measurements. Test specimens were laser cut in three directions referenced to the rolling direction: longitudinal (L), diagonal (D), and transverse (T). The geometry of the samples can be found in Pérez Caro et al. [17]. The tests were performed at a strain rate range of  $1.4 \times 10^{-3} - 4.0 \times 10^{-3} \text{ s}^{-1}$  and temperature range of 20–1000 °C, conforming to the ISO 6892-1:2009 and ISO 6892-2:2011 standards. Each target temperature, i.e. 150, 300, 500, 700, 800, 900, 950, and 1000 °C, was reached using inductive heating. The temperature was measured until fracture using two different Optris CT pyrometers, LT22 (150–700 °C) and 3MH2 (800–1000 °C), pointed at the centre of the surface of each specimen. The emissivity was previously calibrated against a type-K thermocouple at each target temperature with a maximum error < 1%. The distribution of the temperature along the evaluation length, at the start of selected tests, was measured using a FLIR T440 infrared camera. The variation was, in all cases, between 0.5 and 1% of the corresponding target temperature.

A temperature-resistant stochastic pattern was painted on the surface of the samples to measure and compute the deformations during the tests using a facet size/step of  $19 \times 15$  pixels and a frame rate range of 20–4 Hz. The flow curves for alloy 718 in Fig. 5a were obtained after the evaluation of

the strain-localisation area before fracture, with an average size of  $4 \times 5 \text{ mm}$ . The true stresses were calculated from the force measurements whereas the true strains were computed from the strain measurements with DIC. A more detailed description of the strain evaluation procedure using DIC can be found in [32]. The abrupt change in the slope of the hardening curves at 900, 950, and 1000 °C is due to the variation in strain rate during the test. Due to the presence of serrations, and the need to acquire smooth and continuous input data into the FE simulations, the hardening curves were smoothed using a user-defined code based on the smoothing-spline function in MATLAB R2014b, as illustrated in Fig. 5b.

The experimental mechanical properties of alloy 718 between 20 and 1000 °C, calculated from the smoothed curves, are listed in Table 1. The Young's moduli (E) were previously determined by Pérez Caro [31] by the impulse excitation technique (IET) [33] between 20 and 700 °C, whereas the elastic data at higher temperatures, up to 1000 °C, were extracted from JMatPro®-V9. The Young's modulus was used as a reference for determining the initial yield stresses at each temperature. The biaxial yield stress of alloy 718 at 20 °C, obtained by the silicone-rubber bulge test [34] by Pérez Caro et al. [17], was used to scale the biaxial yield stresses between 150 and 1000 °C, following the same tendency as in the yield stresses obtained from the uniaxial tensile tests in the longitudinal direction. The Lankford coefficient, in the biaxial stress state, is assumed equal to one at all temperatures.

The variation of the Young's modulus with temperature and strain was determined through loading–unloading tests using the same test setup as for the uniaxial tensile tests.

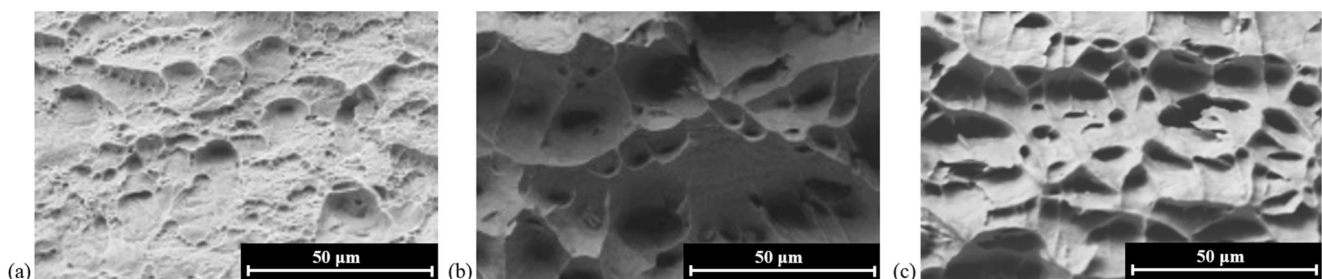
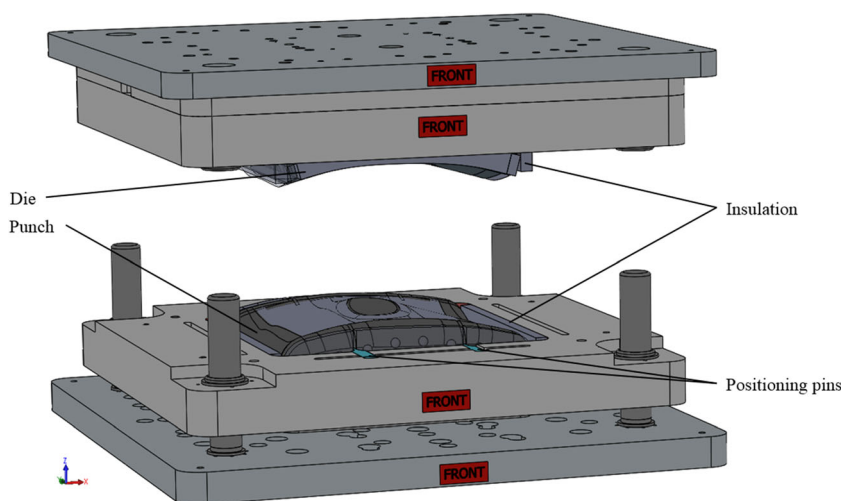


**Fig. 8** Fracture surfaces of the tested tensile specimens at (a) 20 °C, (b) 700 °C, and (c) 1000 °C

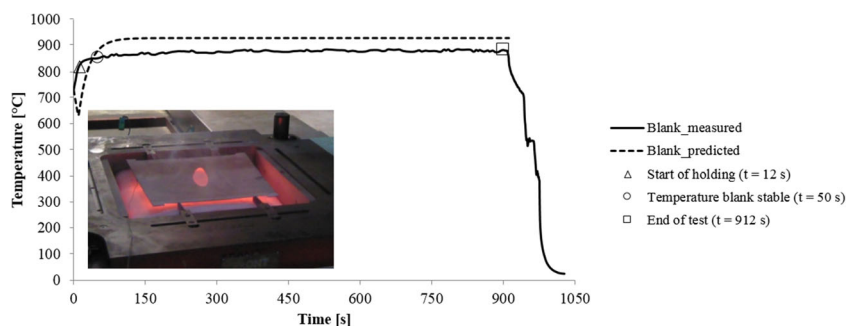
**Fig. 9** Hot forming tooling (CAD), with the formed part, punch, die, insulation material, and positioning pins. The heating cartridges are placed inside the holes in both the punch and die



Every specimen was unloaded at different strain levels according to the displacement sensor in the tensile test machine, i.e. 3%, 8%, 11%, and 19%. The flow curves were obtained from an evaluation area of approximately  $50 \times 8$  mm. The Young's modulus at each target temperature in Table 1 was scaled according to the corresponding percentage variation found from the loading–unloading tests. Table 2 lists the calculated Young's moduli as a function of temperature and strain.

Stress relaxation tests were performed, in the L direction, at a strain rate of  $1.4 \times 10^{-3} \text{ s}^{-1}$  between 800 and 900 °C. The specimens were tested, using the MTS equipment, up to an engineering strain of 3%, and held at those positions while the force, i.e. stress reduction, with time was recorded. The occurrence of stress relaxation in the elastic region for alloy 718 at high temperatures was assumed as a similar behaviour as reported by Odenberger et al. [3] during the hot forming of Ti-6Al-4 V. Each curve was smoothed and extrapolated up to 900 s using a user-defined code in MATLAB R2017a. Figure 6 shows both the experimental and smoothed curves. The difference between the true stresses at the beginning and end of each stress relaxation curve yielded a scale factor of 0.257, which was implemented in a user-defined code in Fortran 77 to scale down the residual stresses obtained from the hot forming FE simulation. The transformed stress state was used as input to the subsequent springback FE analysis.

**Fig. 10** Measured and predicted temperature of the blank during the hot forming process, including holding and cooling to room temperature. The blank is placed on support pins with the thermocouple attached to its left edge



## Microstructural examinations

Figure 7 shows the typical microstructure of alloy 718, obtained from an optical microscope, after testing at 20, 700, and 1000 °C. The samples were extracted at a small distance from the fracture zone, after which they were polished with 3  $\mu\text{m}$  diamond paste, and finally etched with oxalic acid at 2.6 V. The tested specimens at 20, 700, and 1000 °C presented almost no variation in grain sizes. However, there was a noticeable increment and coarsening of the grain boundary precipitates with temperature. The irregular grain edges and strain lines inside some of the grains suggest dynamic recrystallization at 1000 °C.

The microstructure of the fracture surfaces from the uniaxial tensile tests was studied by scanning electron microscopy (SEM). The chemical elemental composition was analysed with energy-dispersive X-ray spectroscopy (EDS). Figure 8 shows selected SEM images from the fractured surfaces of the specimens tested at 20, 700, and 1000 °C.

## Validation test

A crash-forming test at elevated temperature was performed to validate the predicted shape distortions and temperatures from the FE simulations. The tool used for the forming experiments at room temperature by Pérez Caro [31] was modified for this

**Table 3** Average surface temperatures in the four different zones of the punch (P) and die (D)

Zone	Temperature [°C]
P1	839.9
P2	899.8
P3	924.9
P4	959.7
D1	847.4
D2	925.8
D3	928.9
D4	962.8

purpose. The punch and die were heated up to the desired forming temperature using 36 UTX electrical cartridge heaters, with power ranges from 2000 to 2500 W each, strategically placed inside each tool part to obtain an evenly distributed temperature on the surface. Figure 9 illustrates the hot forming test setup. The punch and die were thermally insulated preventing heat transfer to the surrounding tool parts.

The forming test was carried out using a Wemhöner hydraulic press with 1300 tons of press capacity. A type-K thermocouple was welded on the left edge of the blank to measure its temperature during the heating and forming process, as shown in Fig. 10. The blank was placed on support pins, and the die was moved closer to the punch to heat the blank up to 900 °C. When the temperature of the part was stable, the die returned to its start position and the forming test was initiated, see Fig. 10. The initial forming temperature was 728.4 °C. The component was formed at a velocity of 5 mm/s and a stamping force of 1500 kN, followed by a holding time of 900 s in the closed-tool position. The measured temperature of the component, at the end of the hot forming process, was 881.5 °C. The average temperature of

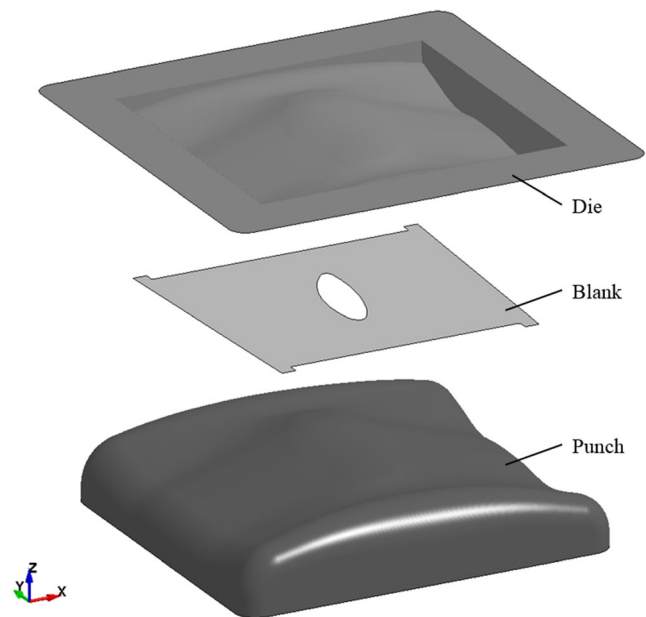


**Fig. 12** FE model of the hot forming procedure in alloy 718

the blank, between the start of the hot forming procedure and end of holding, was 872.6 °C. After the forming process, the part was allowed to air cool to room temperature.

The distribution of the temperature on the surface of the punch, die, and blank was measured using the thermal camera. An emissivity factor of 0.80 was determined by comparison of the thermal images with the measured temperature of the blank at the end of the heating stage. The blank, punch, and die were previously coated with boron nitride to avoid reflections that could affect the measurements with the thermal camera. The surface temperature of the tool parts in Fig. 11a and b corresponds to the stage before placing the blank on the

**Fig. 11** Thermal images of the (a) punch and (b) die before the heating stage of the blank, prior to the forming procedure; (c) and (d) the corresponding thermal zones, P1 – P4 and D1 – D4

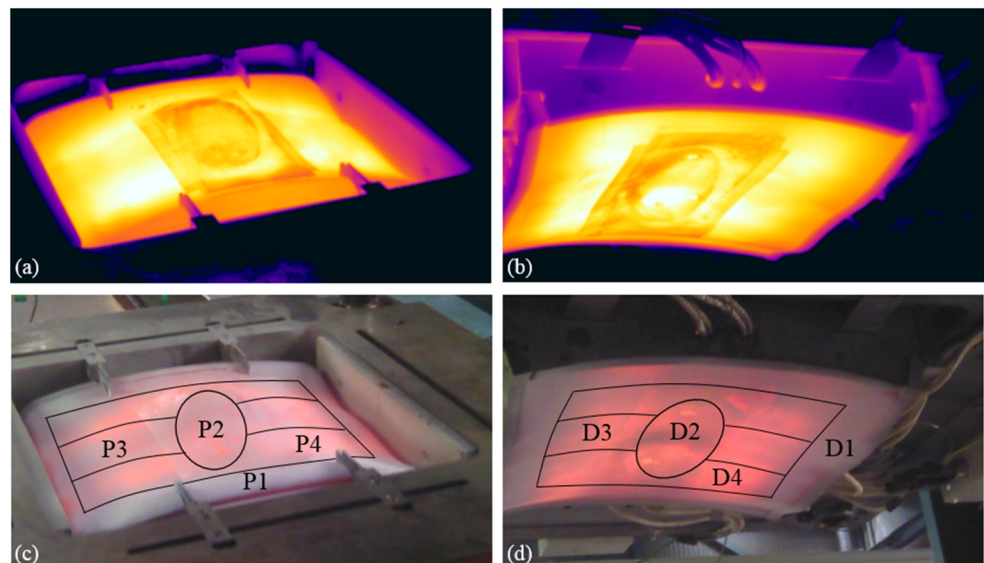




**Table 4** Barlat Yld2000-2D anisotropic parameters ( $\alpha_i$ ) for alloy 718 between 20 and 1000 °C. The data at 20 °C is extracted from Pérez Caro [31]

Temperature [°C]	$\alpha_1$	$\alpha_2$	$\alpha_3$	$\alpha_4$	$\alpha_5$	$\alpha_6$	$\alpha_7$	$\alpha_8$
20	0.8693	1.1190	0.8083	0.9929	0.9859	0.8372	1.0010	1.1580
150	0.9105	1.0490	0.8229	0.9875	0.9841	0.8371	0.9901	1.1680
300	0.9385	1.0040	0.8591	0.9749	0.9812	0.8320	0.9814	1.1220
500	0.9489	1.0090	0.8625	0.9728	0.9786	0.8377	0.9794	1.0880
700	0.9352	1.0340	0.8421	0.9798	0.9800	0.8416	0.9978	1.1250
800	0.8993	1.0830	0.8123	0.9908	0.9836	0.8421	1.0240	1.2270
900	0.9365	1.0450	0.8428	0.9791	0.9785	0.8453	1.0740	1.3330
950	0.9991	0.9458	0.9013	0.9585	0.9724	0.8399	1.0450	1.2420
1000	0.6411	1.5490	0.5618	1.0820	0.9978	0.8705	1.2140	1.7980

positioning pins. Four different temperature zones were differentiated in each part, see Fig. 11c and d, as listed in Table 3.

The total amount of springback was measured, after the hot forming process, via 3D scanning. The scanned part was compared with the CAD nominal geometry using a best-fit evaluation.

### Numerical procedure

The FE analysis of the manufacturing process of the double-curved component made of alloy 718 consists of a crash-forming procedure, including heating, crash-forming, and holding allowing for stress relaxation, followed by

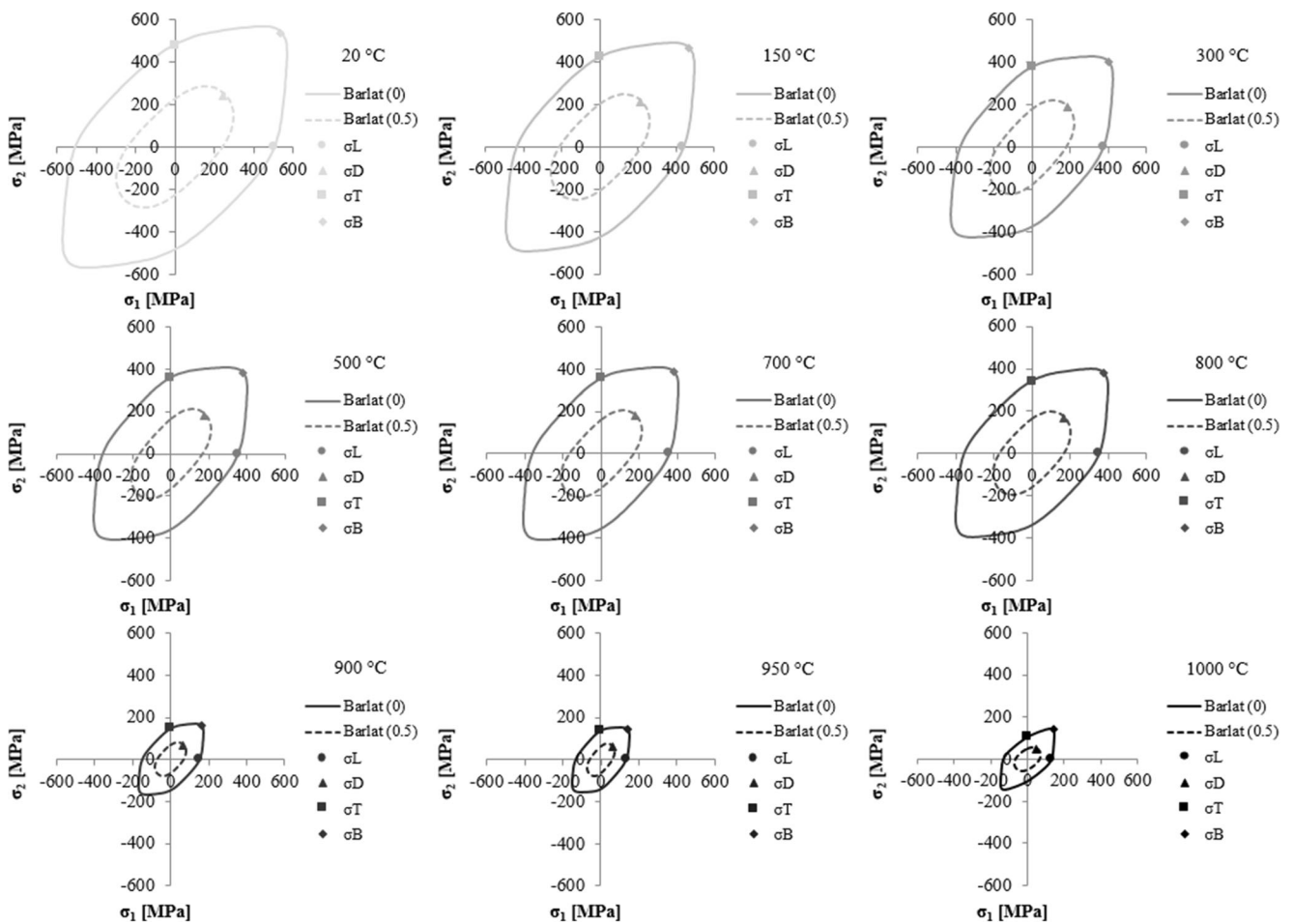


**Fig. 13** Calibrated yield surfaces for alloy 718 between 20 and 1000 °C. The curves correspond to 0 and 0.5 shear stress values. The experimental yield stresses ( $\sigma$ ) for the three rolling directions tested (L, D, and T), and in the B stress state, are included, c.f. Table 1

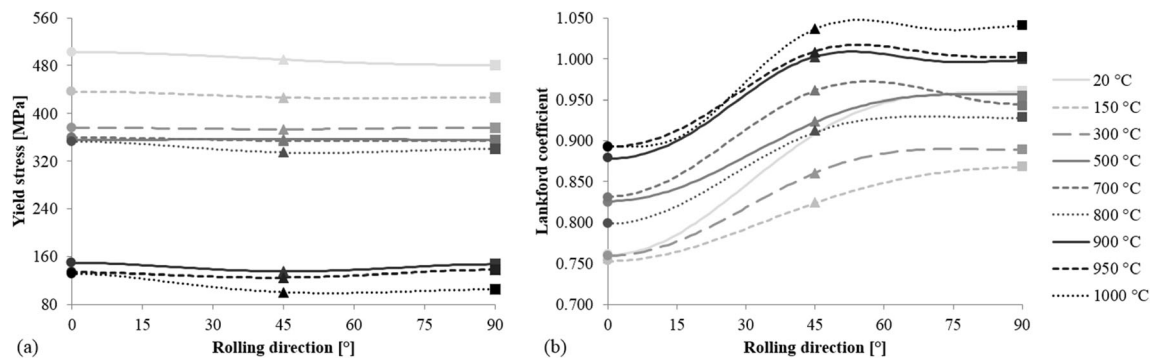


**Fig. 14** Variation of (a) yield stresses and (b) Lankford coefficients with rolling direction for alloy 718 between 20 and 1000 °C. The experimental data are referenced to the L (0°), D (45°), and T (90°) directions

springback. The virtual tool setup was created in Dynaform v5.9.3 from the initial graphics exchange specification (IGS) surfaces obtained via a three-dimensional (3D) scan of the physical tool. Figure 12 illustrates the FE model, which includes the die, blank, and punch. The tool setup included 250,584 nodes and 249,946 elements. The hot forming simulation was analysed using a coupled thermo-mechanical approach in LS-DYNA R11.0.0 [35], i.e. the explicit and implicit solvers for the mechanical and thermal calculations, respectively. The tool parts were modelled as rigid. The die travelled at a velocity of 500 mm/s, corresponding to a scale factor of 100, in the negative z-direction based on a prescribed velocity profile. A static and dynamic coefficient of friction of 0.40 was assumed and modelled using the Coulomb's friction law in the mechanical contact between the blank, punch, and die. Several authors have used similar values of the friction coefficients, ranging from 0.42 to 0.45, in the press hardening of boron steel [36] and hot stamping of high-strength steel [37], respectively, yielding promising agreement with experimental results.

The model of the blank consisted of 250,582 nodes and 33,992 square shell elements. The element size was 2 mm. The element formulation was fully integrated (type 16) with four and seven integration points in-plane and through the thickness, respectively. The novel version of the Yld2000 material model by Barlat [16], which considers thermo-

mechanical data, was used to model the behaviour of the component during the hot forming process. The input data needed to calibrate the model was obtained from the non-destructive, uniaxial tensile, and bulge tests, c.f. Table 1. The variation of the shape of the yield surface with temperature is shown in Fig. 13. The corresponding  $\alpha$  parameters that determine each yield surface are listed in Table 4. The variations of the initial yield stresses and Lankford coefficients depending on the rolling direction are illustrated in Fig. 14. As recommended by Barlat and Lian [38] for FCC materials, the flow potential exponent in the definition of the yield function is assumed to equal 8.

The simulation software JMatPro®-V9 was used to obtain the variation of the density, Poisson's ratio, thermal conductivity, and specific heat with temperature for the specific batch of alloy 718. A constant density of 7938 kg/m<sup>3</sup> was assumed throughout the forming process, corresponding to an average temperature of the blank of 872.6 °C. The corresponding thermal properties for both the tool [39] and blank materials employed in the model are shown in Fig. 15. The heat transfer coefficient (HTC) of each tool part, i.e. punch and die, was calculated as the corresponding thermal conductivity of 30 W/mK at 950 °C divided by its average thickness, being 132.2 and 46.6 mm, respectively. Thus, the HTC between the blank and punch was 227.008 W/m<sup>2</sup>K while 643.181 W/m<sup>2</sup>K between the blank and die.

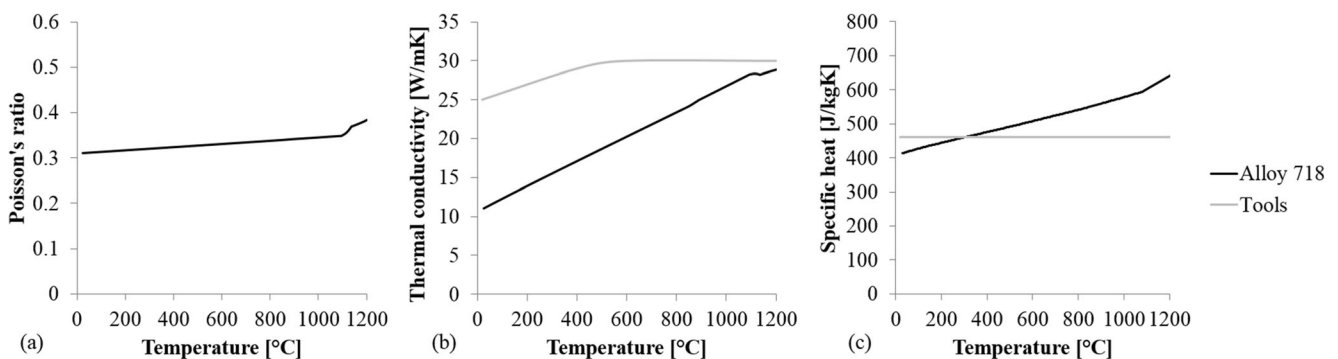
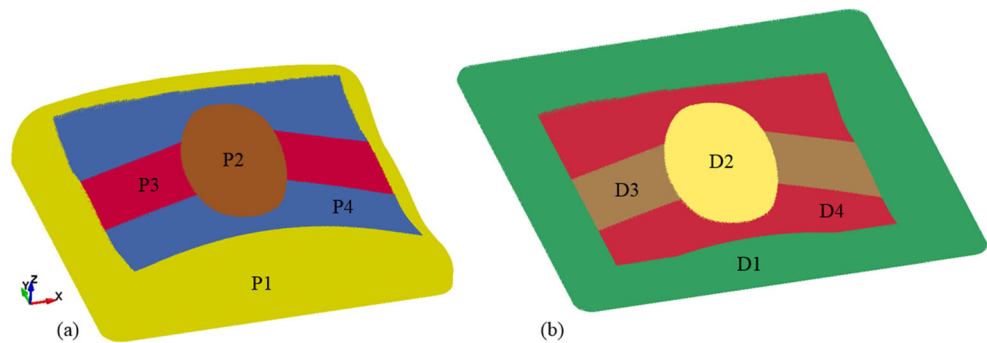


**Fig. 15** a Poisson's ratio, b thermal conductivity, and c specific heat for the blank and tools [39] obtained from JMatPro®-V9 for the specific batch of alloy 718

**Fig. 16** Average nodal temperatures in the (a) punch and (b) die used in the FE analyses, c.f. Table 3



As illustrated in Fig. 11, the four different temperature zones in each tool part were mapped to the respective nodes in the FE model, see Fig. 16.

After the forming process, the springback analysis was set up in LS-PrePost v4.5.25 using the nodal constraints in Fig. 17. The springback simulation was performed using the implicit solver in LS-DYNA R11.0.0.

## Results and discussion

The calibrated yield surfaces for alloy 718 between 20 and 1000 °C in Fig. 13 show that the yield surface progressively reduces its area with temperature while maintaining its original shape, except at 1000 °C. The yield stresses decrease with temperature in all cases and rolling directions, except for the longitudinal case at 700 °C, c.f. Table 1 and Fig. 14a. The degree of anisotropy in strain tends to weaken with increasing temperature, except at 1000 °C, where the anisotropy in stress increases. However, a yield stress plateau can be noticed between 500 and 800 °C for the L-direction case, comparable to the results by Weaver et al. [22] between 227 and 627 °C. A qualitative analysis of the EDS measurements at 20, 700, and 1000 °C showed a progressive reduction in the chemical elemental composition of Nb, Mo, Ti, and Al with temperature, see Fig. 18. A decrease in the concentration of Nb and Ti at 700 °C suggests the presence of additional  $\gamma'$  and  $\gamma''$  precipitates. As concluded by Rezende et al. [27], the increase in the yield stress at 700 °C can be related to the depletion of solute elements that precipitate in the forms of  $\gamma'$  and  $\gamma''$  phases, which are responsible for the precipitation hardening. Figure 19 shows the time-temperature-transformation (TTT) diagram, extracted from JMatPro®-V9, for the specific batch of alloy 718. Both the  $\gamma'$  and  $\gamma''$  phases are more likely to precipitate, i.e. at 700 °C, than  $\delta$  phase. The loss of ductility can be attributed to the onset of the OAIC phenomenon, as reported by Zang et al. [40] between 800 and 950 °C.

The different micrographs illustrated in Fig. 7 reveal that the grain size distribution remains practically constant between 20 and 700 °C. Weaver and Hale [22] and Maj et al. [28] experienced no significant changes in the microstructure

of alloy 718 when exposed at temperatures up to 627 and 700 °C, respectively. The presence of small dimples on the fracture surfaces in Fig. 8a indicates ductile fracture by coalescence of microvoids at 20 °C. As appointed by Rezende et al. [27], intergranular or crystalline fracture was dominant in the sample tested at 700 °C, see Fig. 8b. The fewer but larger dimples, compared to those in the sample at 20 °C, imply less ductility. The same tendency was observed in Fig. 8c for the tested specimen at 1000 °C.

The DSA phenomenon is clearly present between 300 and 800 °C owing to serrations in the true stress–strain curves. The frame rate of 4 Hz used in the DIC system was in the lower region of the requirements to detect and identify serrations, c.f. Figure 5a. The force response was instead extracted from the MTS tensile test machine, at a high frame rate of 100 Hz, to confirm the type of serrations. The amplified view of the corresponding curves in Fig. 20 illustrates the different types of serrations found at those temperatures. Even though the serrations were, in all cases, accompanied by an audible sound, the qualitative analysis of both their frequency and amplitude yielded three different types of yield drops. As reported by Maj et al. [28], both the frequency and amplitude of the yield drops increase with temperature owing to an increase in the interaction between solute atoms and mobile dislocations. Considering the 300 °C case, A-type serrations occurred at low strain values, whereas B-type serrations appeared near the end of the test. Purely B-type serrations were present at

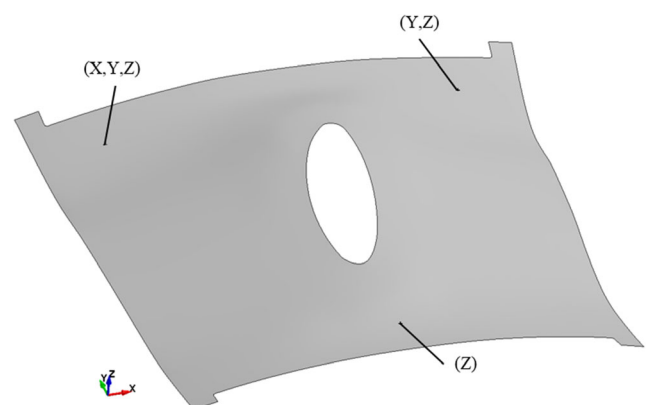


**Fig. 17** Nodal constraints considered in the springback calculations



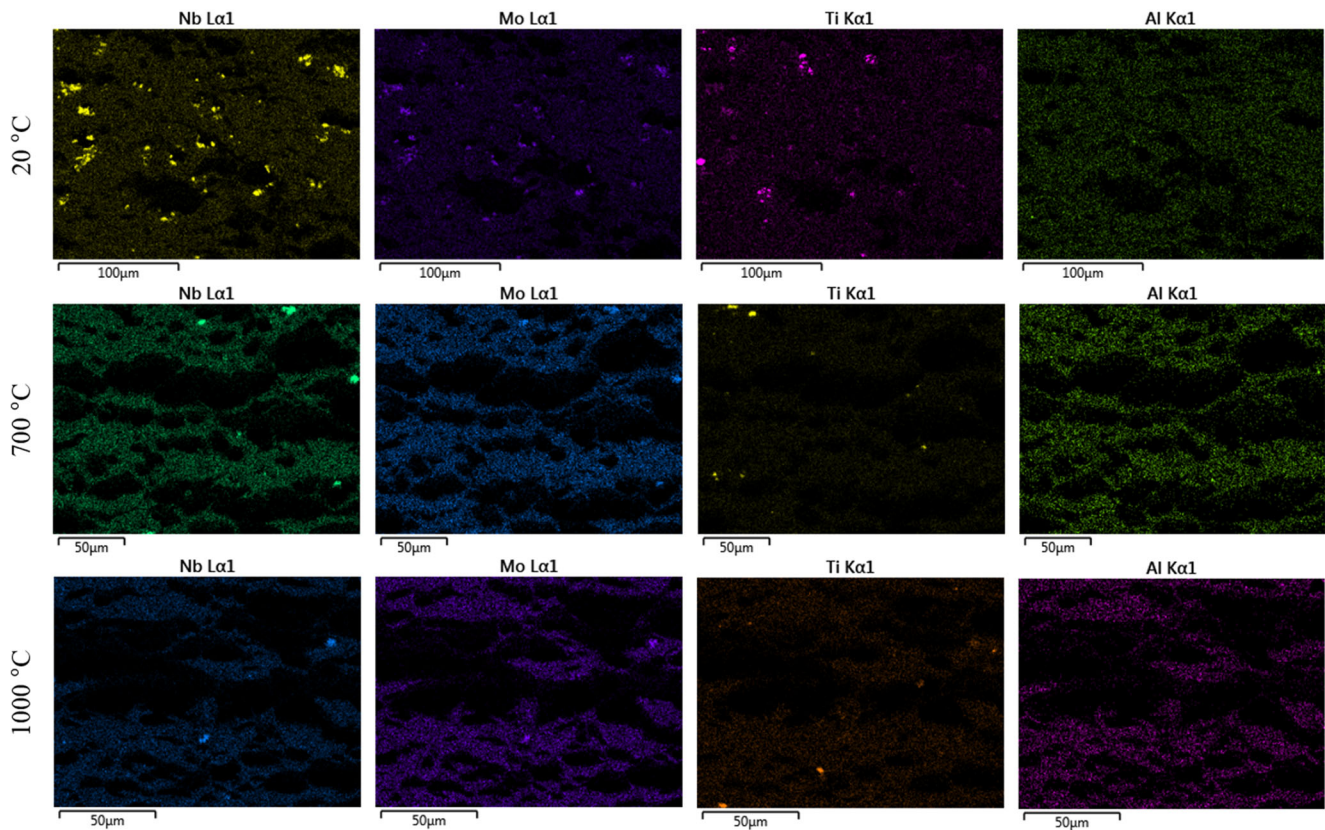


**Fig. 18** EDS measurements of the fracture surfaces from the uniaxial tensile tests of alloy 718 at 20, 700, and 1000 °C

500 °C. The specimens tested at 700 and 800 °C showed C-type serrations, with yield drops below the general level of the curve. No serrations were observed at 900, 950, or 1000 °C.

The temperature ranges, where certain types of serrations were dominant, are in accordance with other studies available in literature at similar strain rates. Weaver and Hale [22] and Rezende et al. [27] determined that A- and B-type serrations are usually found between 200 and 450 °C. Nalawade et al. [24] and Hayes [25] distinguished the temperature ranges of A- and B-type serrations, i.e. 200 and 300–450 °C, respectively. C-type serrations are dominant between 450 and 760 °C [22, 24, 27]. In a further work by Nalawade et al. [26], A-type serrations were observed at 300 °C, whereas B- or A + B-type serrations were observed between 400 and 600 °C. C-type serrations were found at 650 °C. Similar conclusions were

reported by Maj et al. [28], with A-type serrations at 250 °C, B-type serrations at 300 °C, and C-type serrations between 300 and 750 °C. These temperature ranges may vary due to several factors, such as the test method, strain rates, or small variations in the heat treatment of the material.

The microstructural effect of the DSA phenomenon is usually related to the interactions between interstitial or substitutional solutes with mobile dislocations. The agreement of Weaver and Hale [22] and Maj et al. [28] on A- and B-type serrations can be attributed to the interaction between interstitial solutes and moving dislocations. Furthermore, substitutional solute diffusion, i.e. Nb, is the common cause of C-type serrations. The disappearance of serrations after some time at 700 and 800 °C, c.f. Figure 5a, and at higher temperatures, could be explained through the reduction of interstitial

**Fig. 19** TTT diagram of the specific batch of alloy 718

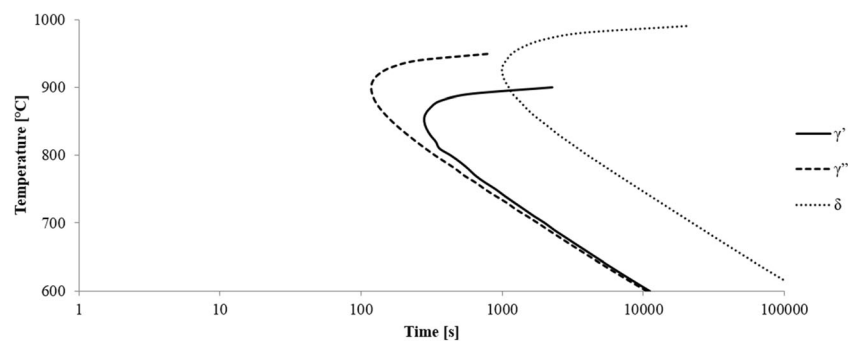
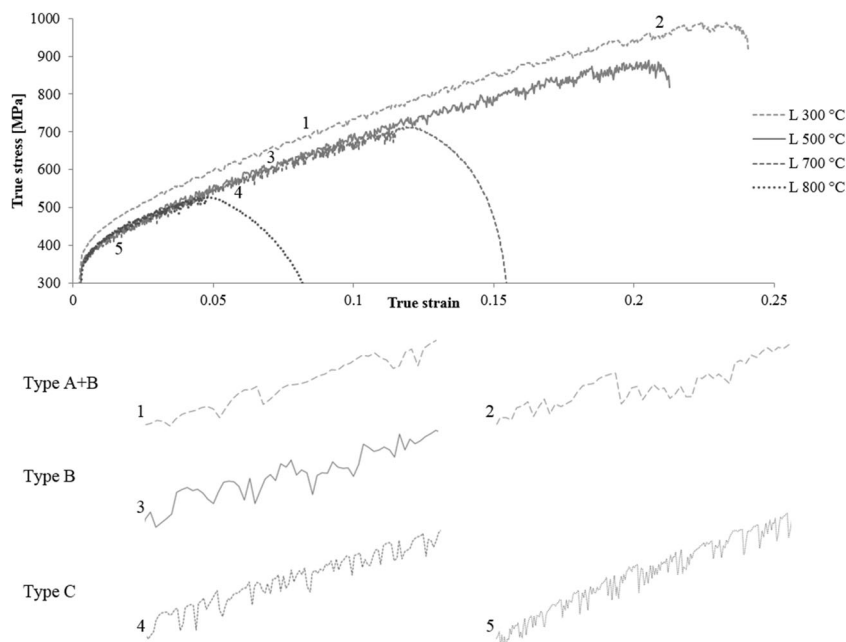




**Fig. 20** Different types of serrations found between 300 and 800 °C from MTS measurements. The amplified view of each type of serration is marked with 1–5 in the corresponding area of the curve



and substitutional solutes due to precipitation at the grain boundaries, which consequently prevents the occurrence of DSA [22, 24–28]. Fisk et al. [41] studied the precipitate evolution in the early stages of aging in a solution-annealed alloy 718. Aging was carried out at temperatures between 500 and 850 °C for different times, ranging from 4 to 480 min. They concluded that the size and distribution of  $\gamma''$  precipitates increased for relatively long aging times, with clear evidence of  $\gamma''$  precipitates presented when aging for 8 min at 760 °C. Therefore, an increase in the number and size of  $\gamma''$  precipitates could be expected in the double-curved component after the holding time of 900 s at 872.6 °C. The evolution of the critical strain for the onset of serrations with temperature is illustrated in Fig. 21. The critical strain decreased with increasing temperature (normal behaviour), following a tendency to increase with increasing temperature (inverse behaviour) [22, 24, 42, 43]. The transition from the normal to inverse

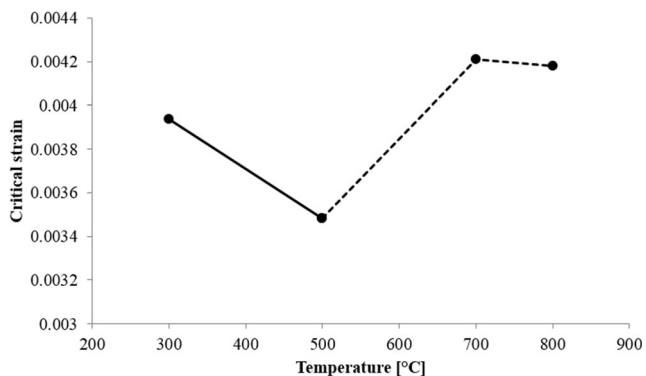


**Fig. 21** Variation of the critical strain for the onset of serrations with temperature. The solid and dashed lines indicate normal and inverse behaviour, respectively

behaviour, at 500 °C, coincided with the change from A- and B-type to C-type serrations, respectively.

Figure 22 shows the predicted effective plastic strains at different stages of the forming process, i.e. after tool closure and start of holding ( $t = 12$  s), when the measured temperature of the blank has been stable ( $t = 50$  s), and at the end of the hot forming test including the holding time of 900 s ( $t = 912$  s). The corresponding predicted temperature distribution over the part is illustrated in Fig. 23. The predicted temperature at the same position as where the type-K thermocouple was placed on the specimen is included in Fig. 10 for comparison purposes. The temperature in the blank starts to normalise, according to the different temperature zones in Fig. 16, from  $t = 50$  s. The results are presented for the integration point located in the middle of the thickness of each shell element. The highest plastic strains are located at the upper part of the central hole. Plastic strains ranging between  $10^{-2}$  and  $10^{-3}$  are concentrated along the central y-axis. The overall effective plastic strains  $\leq 10^{-4}$  indicate that the component was mostly formed under elastic conditions.

The maximum residual stress level over the part decreases by 46% when the temperature is stable, and by an extra 6% at the end of the holding stage, see Figs. 24a – c. The springback simulation in Figs. 24d – f further decreases the residual stresses over the part. The consideration of the data from the stress relaxation tests significantly reduces the amount of residual stresses, as illustrated in Fig. 25a – c. The von Mises stresses after springback are depicted in Figs. 25d – f.

Figure 26 a – c show the predicted shape deviations after springback for the three considered cases, c.f. Figure 24d – f. The effect of the stress relaxation from Fig. 25d – f on the corresponding numerical results is illustrated in Fig. 27a – c.

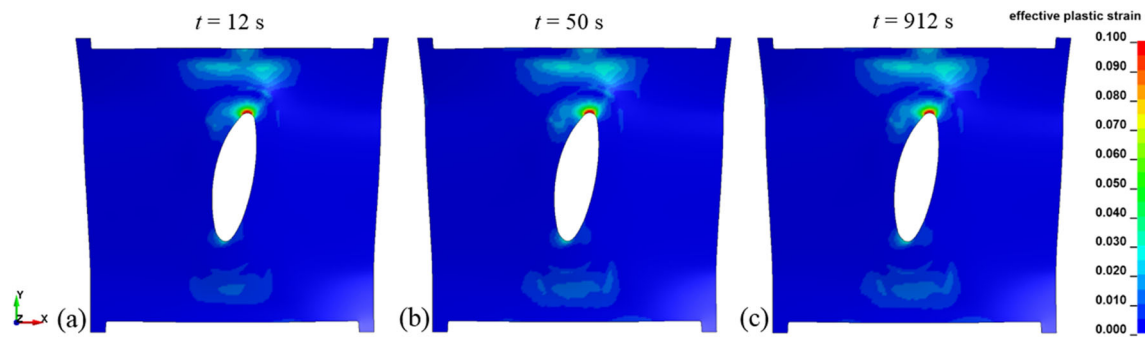


Fig. 22 Effective plastic strains at different stages of the hot forming procedure

The measured amount of springback in the hot-formed part is presented in Fig. 28 for comparison

The predicted springback after hot forming without considering the holding time ( $t = 12$  s) in Fig. 26 a considerably deviates from the 3D-scanned part, c.f. Figure 28. The overall distortions when the temperature of the blank is stable ( $t = 50$  s) range between 1 and 2 mm, except in the four protruding areas, where the shape deviations considerably exceed the thickness of the sheet. As illustrated in Fig. 27, the distribution and degree of shape distortions after considering stress relaxation are in much better agreement with the experimental measurements. However, the springback results at  $t = 12$  s in Fig. 27a present the highest deviances in almost all measurement points up to 1.119 mm. The predicted shape deviations at  $t = 50$  s are the closest to the measured values, particularly at the right and left sides of the component, see Fig. 27b. On the contrary, the predicted amount of springback at the end of the forming test, including the holding time of 900 s ( $t = 912$  s), better agrees at the top and bottom areas, as well as the ear-shaped corners, see Fig. 27c. The maximum difference between the simulations and experiment was  $\leq 0.886$  mm and  $\leq 0.756$  mm, respectively.

The hot deformation and springback behaviour of alloy 718 can strongly be related to its mechanical properties. By comparison with the study by Odenberger et al. [3] about hot forming of Ti-6Al-4 V, the Young's modulus of alloy 718, obtained via IET tests, is approximately 50% lower than Ti-6Al-4 V at 700 °C. These results indicate that the amount of

springback in alloy 718 could be expected to be lower than Ti-6Al-4 V at the considered temperature. However, the lack of serrations of Ti-6Al-4 V suggests that the formability should be better than in alloy 718 up to 700 °C, where the DSA phenomenon was clearly present between 300 and 800 °C.

The yield stress also influences the amount of elastic deformation that occurs during the hot forming procedure and thereby the amount of springback obtained. The yield stress decreases, from 20 to 700 °C, approximately 70% [3] and 28% for Ti-6Al-4 V and alloy 718, respectively. The yield stress of Ti-6Al-4 V at 700 °C is 296.10 MPa, about 18% lower than alloy 718. The flow curves of alloy 718 in Fig. 5 present a pronounced work hardening behaviour compared to Ti-6Al-4 V from Odenberger et al. [3] at all temperatures. The higher Lankford coefficient and elongation to fracture values of alloy 718, compared to Ti-6Al-4 V between 20 and 700 °C in the longitudinal direction with respect to the rolling direction, suggest a better formability for alloy 718. This is in good agreement with the well-known low formability of Ti-6Al-4 V between room temperature and up to about 500 °C.

Odenberger et al. [3] concluded that Ti-6Al-4 V was sensitive to stress relaxation at temperatures over 400 °C, with low stress relaxation rates at 500 and 600 °C. Major stress relaxation could be observed at 700 °C in both the elastic and plastic regions, corresponding to a suitable temperature for hot forming while applying a subsequent holding time to significantly reduce springback. However, the stress relaxation curves of alloy 718 in Fig. 6 show a quite low stress relaxation

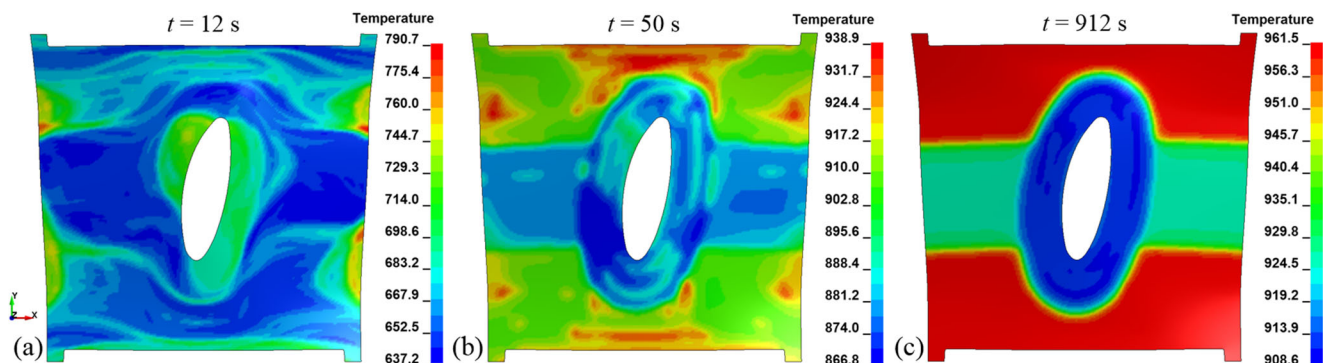


Fig. 23 Predicted temperature distribution at different stages of the hot forming procedure

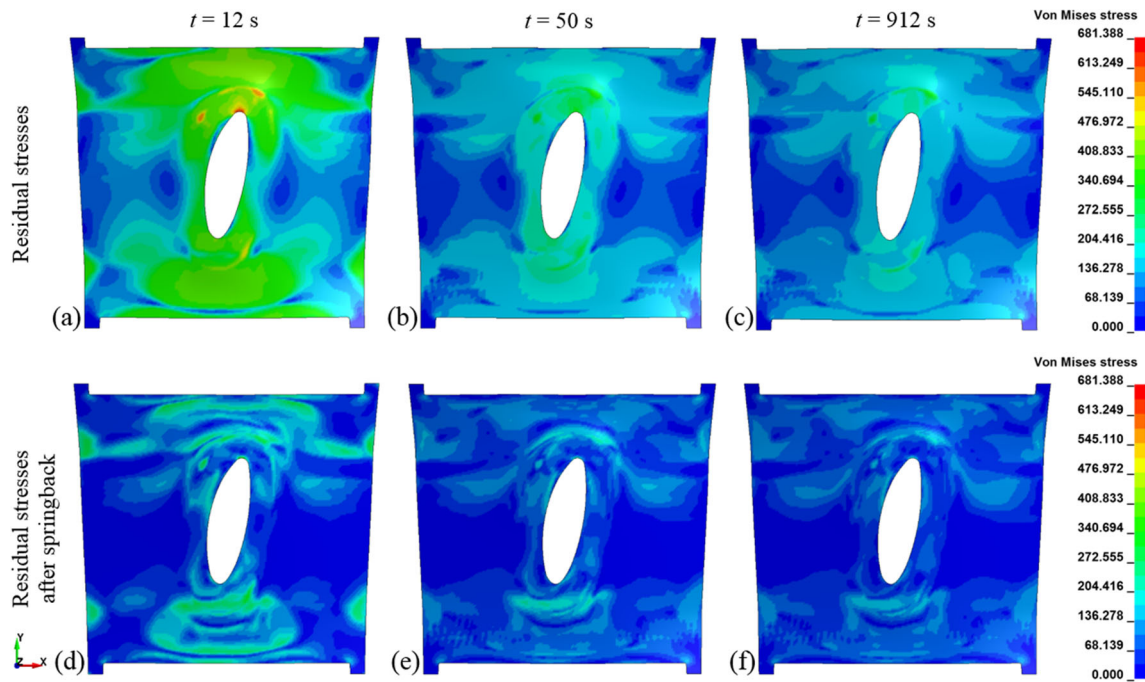


Fig. 24 Von Mises stresses (a) – (c) at different stages of the hot forming procedure and (d) – (f) after springback

rate at 800 °C. Therefore, a higher forming temperature is required for alloy 718 to reach a suitable level of stress relaxation for hot forming, mainly due to the DSA phenomenon and stress relaxation behaviour of the material.

The deviances between the measured and simulated shape deviations may originate from the selection of the scale factor to transform the residual stresses. Since the scale factor

controls both the magnitude and speed of the residual stress relaxation process with time, it may affect the predicted springback. In this work, the scale factor for each stress relaxation test in Fig. 6 was calculated based on the corresponding initial temperature and strain level. The scale factor of 0.257 was obtained by linear interpolation and assuming a constant temperature of the blank, 872.6 °C. Variations in the nodal

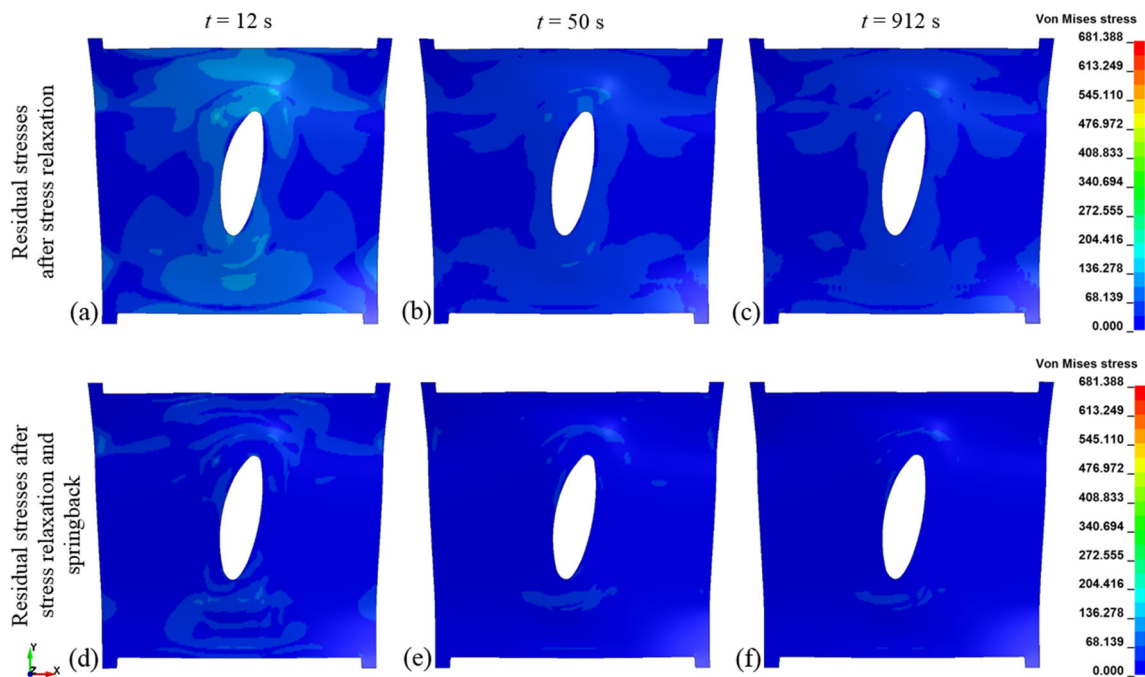
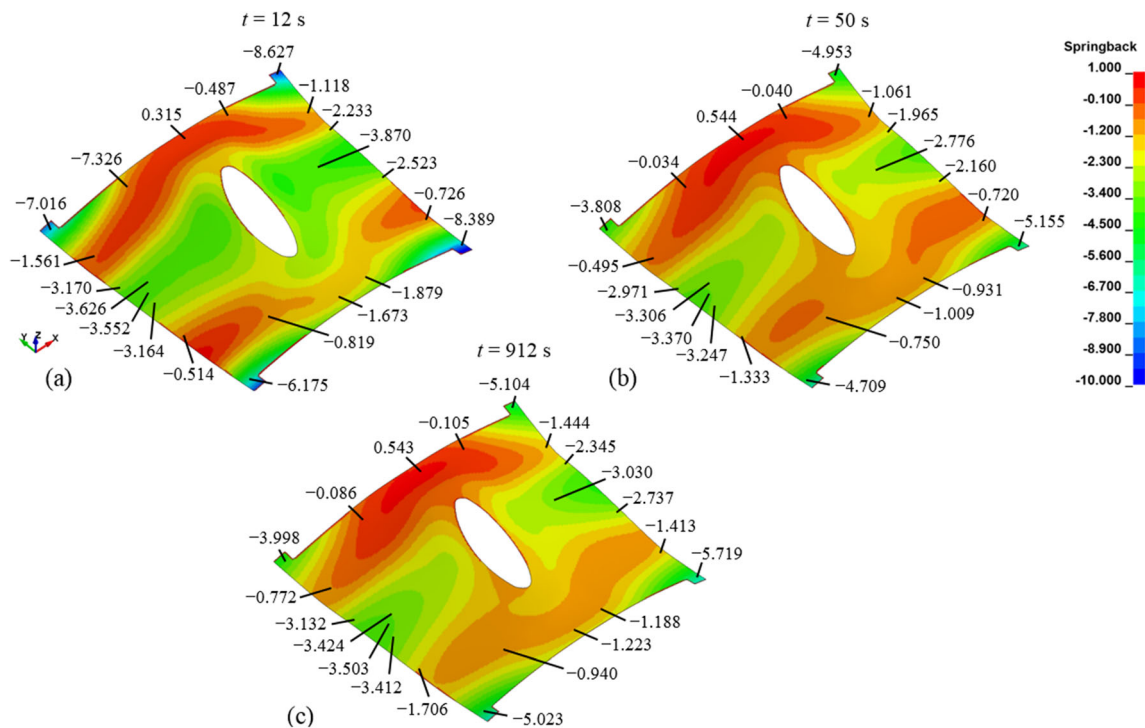


Fig. 25 Von Mises stresses (a) – (c) at different stages of the hot forming procedure considering stress relaxation and (d) – (f) after springback



**Fig. 26** Predicted shape distortions at different stages of the hot forming procedure after springback. All measurements are expressed in millimetres

temperatures of the blank will influence the rate and degree of stress relaxation in those areas and, consequently, the shape distortions over the part. Being able to measure and predict the temperature distribution on the surface of the blank during the whole hot forming procedure with high accuracy will allow

the use of suitable scale factors to transform the residual stresses at each node. In addition, the stress relaxation tests were performed at an initial strain level of 3%, which only covers a small range of the effective plastic strains from the forming simulation, c.f. Figure 22. Therefore, additional tests in the

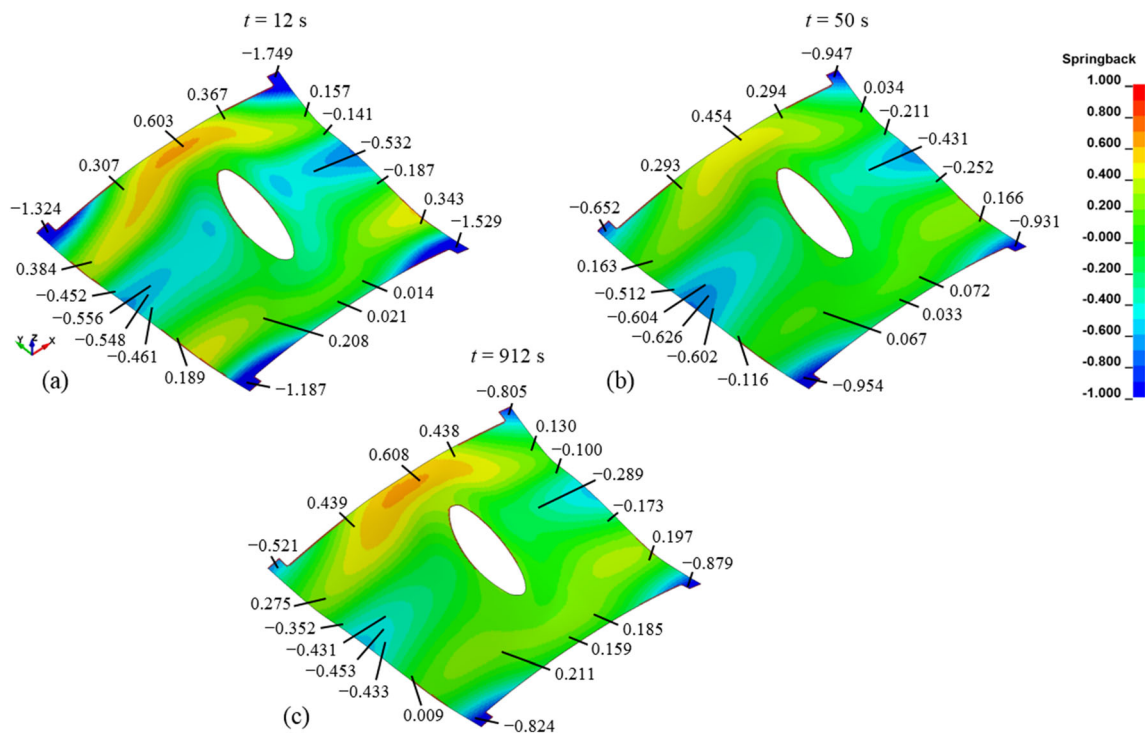


**Fig. 27** Predicted shape distortions at different stages of the hot forming procedure, considering stress relaxation, after springback. All measurements are expressed in millimetres



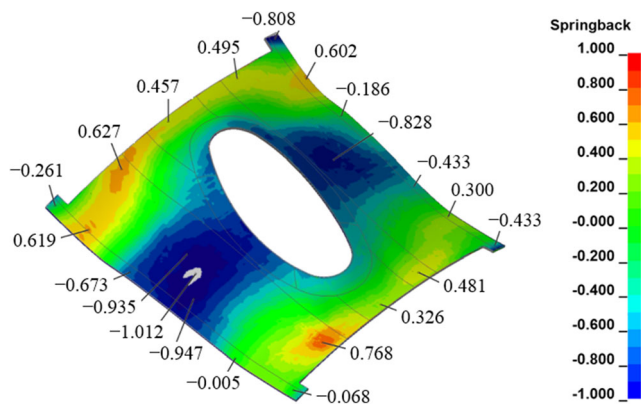


**Fig. 28** Measured springback after the hot forming procedure. All measurements are expressed in millimetres

elastic region and a more advanced method to transform the residual stresses, based on each nodal temperature and strain level, need to be considered. For instance, Odenberger et al. [3] used the Zener-Wert-Avrami function [44] to model the stress relaxation behaviour of a Ti-6Al-4 V alloy during a hot forming procedure at 700 °C.

## Conclusions

In this work, the effect of considering stress relaxation data in the predictions of the final shape of a double-curved component in alloy 718 subjected to a hot forming procedure was studied. The use of accurate thermo-mechanical material data, coupled with advanced FE analyses, yielded the predicted final shape of the component within sheet thickness and acceptable tolerance to the industry. The main conclusions are as follows:

- The sudden increase in the yield stress in the longitudinal rolling direction at 700 °C can be attributed to the precipitation of  $\gamma'$  and  $\gamma''$  phases.
- The DSA phenomenon is present in the material between 300 and 800 °C. Three different types of serrations were identified, i.e. types A and B at 300 °C, type B at 500 °C, and type C between 700 and 800 °C. All serrations were accompanied by an audible sound. The disappearance of serrations at high strain levels at 700 and 800 °C, and at higher temperatures, could be related to the reduction of interstitial and substitutional solutes due to precipitation at the grain boundaries. This is supported by the increase in number and coarsening of precipitates at the grain boundaries shown in the micrographs.
- The shift from normal to inverse behaviour of the critical strain for the onset of serrations at 500 °C coincided with the change from A- and B- to C-type serrations, respectively.

- The predicted springback considering the stress relaxation of the material shows encouraging agreement with the experimental measurements. The tendencies in the distribution of the shape distortions are well captured, with a bit more deviance at the four ear-shaped corners. The maximum shape distortions over the part are less than 25% of the sheet thickness.
- The use of an anisotropic material model coupled with thermo-mechanical analysis, and considering the stress relaxation behaviour, can accurately predict the final shape of a nickel-base superalloy component, which is of interest to the aerospace industry.
- The difference between the predicted and measured springback can be related to the assumption of isothermal stress relaxation whereas the temperature over the part clearly is non-isothermal.
- The consideration of stress relaxation data to simulate the holding stage, during a hot forming procedure, is evidenced to be of utmost importance in the prediction of shape distortions after hot forming with high accuracy. However, there is a need to further develop the method to transform the residual stresses during holding, which considers both the temperature and elastic or plastic strain level at each node.

**Acknowledgments** The authors would like to thank GKN Aerospace Sweden AB, ITE Fabriks AB, DYNAmore Nordic AB, VINNOVA - Swedish Governmental Agency for Innovation Systems NFFP6 program for SME, Swedish Armed Forces, and Swedish Defence Materiel Administration for their support (grant no. 2013-01173).

**Funding** Open Access funding provided by Lulea University of Technology. "This study was funded by VINNOVA – Swedish Governmental Agency for Innovation Systems NFFP6 program for SME, Swedish Armed Forces, and Swedish Defence Materiel Administration (grant number 2013–01173).

## Declarations

**Conflict of interest** The authors declare that they have no conflict of interest.

**Open Access** This article is licensed under a Creative Commons Attribution 4.0 International License, which permits use, sharing, adaptation, distribution and reproduction in any medium or format, as long as you give appropriate credit to the original author(s) and the source, provide a link to the Creative Commons licence, and indicate if changes were made. The images or other third party material in this article are included in the article's Creative Commons licence, unless indicated otherwise in a credit line to the material. If material is not included in the article's Creative Commons licence and your intended use is not permitted by statutory regulation or exceeds the permitted use, you will need to obtain permission directly from the copyright holder. To view a copy of this licence, visit <http://creativecommons.org/licenses/by/4.0/>.

## References

- Mori K, Bariani PF, Behrens BA, Brosius A, Bruschi S, Maeno T, Merklein M, Yanagimoto J (2017) Hot stamping of ultra-high strength steel parts. *CIRP Ann-Manuf Technol* 66(2):755–777. <https://doi.org/10.1016/j.cirp.2017.05.007>
- Zhan L, Lin J, Dean TA (2011) A review of the development of creep age forming: experimentation, modelling and applications. *Int J Mach Tool Manuf* 51(1):1–17. <https://doi.org/10.1016/j.ijmactools.2010.08.007>
- Odenberger EL, Pederson R, Oldenburg M (2019) Finite element modeling and validation of springback and stress relaxation in the thermo-mechanical forming of thin Ti-6Al-4V sheets. *Int J Adv Manuf Technol* 104(9–12):1–17. <https://doi.org/10.1007/s00170-019-04071-9>
- Merklein M, Lechler J (2006) Investigation of the thermo-mechanical properties of hot stamping steels. *J Mater Process Technol* 177(1–3):452–455. <https://doi.org/10.1016/j.jmatprotec.2006.03.233>
- Odenberger EL, Schill M, Oldenburg M (2013) Thermo-mechanical sheet metal forming of aero engine components in Ti-6Al-4V – part 2: constitutive modelling and validation. *Int J Mater Form* 6(3):403–416. <https://doi.org/10.1007/s12289-012-1094-7>
- Åkerström P, Oldenburg M (2006) Austenite decomposition during press hardening of a boron steel – computer simulation and test. *J Mater Process Technol* 174(1–3):399–406. <https://doi.org/10.1016/j.jmatprotec.2006.02.013>
- Åkerström P, Bergman G, Oldenburg M (2007) Numerical implementation of a constitutive model for simulation of hot stamping. *Model Simul Mater Sci* 15(2):105–119. <https://doi.org/10.1088/0965-0393/15/2/007>
- Mori K, Akita K, Abe Y (2007) Springback behaviour in bending of ultra-high-strength steel sheets using CNC servo press. *Int J Mach Tool Manuf* 47(2):321–325. <https://doi.org/10.1016/j.ijmactools.2006.03.013>
- Liu HS, Xing ZW, Bao J, Song BY (2010) Investigation of the hot-stamping process for advanced high-strength steel sheet by numerical simulation. *J Mater Eng Perform* 19(3):325–334. <https://doi.org/10.1007/s11665-009-9510-y>
- Kim HS, Koç M (2008) Numerical investigations on springback characteristics of aluminum sheet metal alloys in warm forming conditions. *J Mater Process Technol* 204(1–3):370–383. <https://doi.org/10.1016/j.jmatprotec.2007.11.059>
- Zhou J, Wang BY, Lin JG, Fu L, Ma WY (2014) Forming defects in aluminum alloy hot stamping of side-door impact beam. *T Nonferrous Metal Soc* 24(11):3611–3620. [https://doi.org/10.1016/S1003-6326\(14\)63506-8](https://doi.org/10.1016/S1003-6326(14)63506-8)
- Xiao WC, Wang BY, Kang Y, Ma WP, Tang XF (2017) Deep drawing of aluminum alloy 7075 using hot stamping. *Rare Metals* 36(6):485–493. <https://doi.org/10.1007/s12598-017-0919-4>
- Abedini A, Butcher C, Rahmaan T, Worswick MJ (2018) Evaluation and calibration of anisotropic yield criteria in shear loading: constraints to eliminate numerical artefacts. *Int J Solids Struct* 151:118–134. <https://doi.org/10.1016/j.ijsolstr.2017.06.029>
- Odenberger EL, Oldenburg M, Thilderkvist P, Stoehr T, Lechler J, Merklein M (2011) Tool development based on modelling and simulation of hot sheet metal forming of Ti-6Al-4V titanium alloy. *J Mater Process Technol* 211(8):1324–1335. <https://doi.org/10.1016/j.jmatprotec.2011.03.001>
- Jeong GU, Park J, Jin CK, Moon YH, Kang CG (2019) Thermal deformation behavior and formability of high temperature with corrosion resistance alloy. *Key Eng Mater* 794:142–150. <https://doi.org/10.4028/www.scientific.net/KEM.794.142>
- Barlat F, Brem JC, Yoon JW, Chung K, Dick RE, Lege DJ, Pourboghrat F, Choi SH, Chu E (2003) Plane stress yield function for aluminium alloy sheets – part 1: theory. *Int J Plast* 19(9):1297–1319. [https://doi.org/10.1016/S0749-6419\(02\)00019-0](https://doi.org/10.1016/S0749-6419(02)00019-0)
- Li PC, Schill M, Haller K, Odenberger EL, Oldenburg M (2019) Damage and fracture during sheet-metal forming of alloy 718. *Int J Mater Form* 12(1):1–14. <https://doi.org/10.1007/s12289-018-01461-4>
- Sims CT, Stoloff NS, Hagel WC (1987) *Superalloys II: high-temperature materials for aerospace and industrial power*. Wiley, New York
- Rodríguez P (1984) Serrated plastic flow. *B Mater Sci* 6(4):653–663
- Portevin A, Le Chatelier F (1923) *C R de l'Acad des Sci Paris* 176: 507–510
- Vandenbrink SH, Vandenbeukel A, McCormick PG (1975) Strain rate sensitivity and the Portevin-Le Chatelier effect in au-cu alloys. *Phys Status Solidi A* 30(2):469–477
- Weaver ML, Hale CS (2011) Effects of precipitation on serrated yielding in Inconel 718. Proceedings of the 5th international symposium on superalloys 718, 625, 706 and various derivatives, Pittsburgh, pp 421–432
- Curtin WA, Olmsted DL, Hector LG (2006) A predictive mechanism for dynamic strain ageing in aluminium-magnesium alloys. *Nat Mater* 5(11):875–880. <https://doi.org/10.1038/nmat1765>
- Nalawade SA, Sundararaman M, Kishore R, Shah JG (2008) The influence of aging on the serrated yielding phenomena in a nickel-base superalloy. *Scr Mater* 59(9):991–994. <https://doi.org/10.1016/j.scriptamat.2008.07.004>
- Hayes RW (1983) On a proposed theory for the disappearance of serrated flow in f.c.c. Ni alloys. *Acta Metall Mater* 31(3):365–371. [https://doi.org/10.1016/0001-6160\(83\)90213-4](https://doi.org/10.1016/0001-6160(83)90213-4)
- Nalawade SA, Sundararaman M, Singh JB, Ramaswamy K, Verma A (2010) Serrated yielding in alloy 718. Proceedings of the 7th international symposium on superalloy 718 and derivatives, Pittsburgh, pp 809–823
- Rezende MC, Araújo LS, Gabriel SB, Dille J, de Almeida LH (2015) Oxidation assisted intergranular cracking under loading at dynamic strain aging temperatures in Inconel 718 superalloy. *J Alloys Compd* 643:S256–S259. <https://doi.org/10.1016/j.jallcom.2014.12.279>
- Maj P, Zdunek J, Gizynski M, Mizera J, Kursydowski KJ (2014) Statistical analysis of the Portevin-Le Chatelier effect in Inconel 718 at high temperature. *Mater Sci Eng A* 619:158–164. <https://doi.org/10.1016/j.msea.2014.09.075>
- Fournier L, Delafosse D, Magnin T (2001) Oxidation induced intergranular cracking and Portevin-Le Chatelier effect in nickel base superalloy 718. *Mater Sci Eng A* 316(1–2):166–173. [https://doi.org/10.1016/S0921-5093\(01\)01224-2](https://doi.org/10.1016/S0921-5093(01)01224-2)
- Garat V, Cloue JM, Poquillon D, Andrieu E (2008) Influence of Portevin-Le Chatelier effect on rupture mode of alloy 718 specimens. *J Nucl Mater* 375(1):95–101. <https://doi.org/10.1016/j.jnucmat.2007.10.009>
- Pérez Caro LL (2019) Modelling aspects in forming and welding of nickel-base superalloys. Dissertation, Luleå University of Technology. ISBN: 978-91-7790-461-8 (digital)
- GOM (2013) ARAMIS v6.3 user manual. GOM Optical Measuring Techniques, Braunschweig
- IMCE (2017) RFDA Professional. <https://www.imce.eu/products/rfda-professional>. Accessed 20 Mar 2019
- Sigvant M, Mattiasson K, Vegter H, Thilderkvist P (2009) A viscous pressure bulge test for the determination of a plastic hardening curve and equibiaxial material data. *Int J Mater Form* 2(4):235–242. <https://doi.org/10.1007/s12289-009-0407-y>
- LSTC (2019) LS-DYNA theory manual. Livermore software technology corporation (LSTC), Livermore
- Deng L, Pelcastre L, Hardell J, Prakash B, Oldenburg M (2019) Numerical investigation of galling in a press hardening experiment

- with AlSi-coated workpieces. *Eng Fail Anal* 99:85–96. <https://doi.org/10.1016/j.engfailanal.2019.01.059>
37. Geiger M, Merklein M, Lechler J (2008) Determination of tribological conditions within hot stamping. *Prod Engineer* 2(3):269–276. <https://doi.org/10.1007/s11740-008-0110-8>
38. Barlat F, Lian J (1989) Plasticity behaviour and stretchability of sheet metals. Part I: a yield function of orthotropic sheets under plane stress condition. *Int J Plast* 5(1):51–56. [https://doi.org/10.1016/0749-6419\(89\)90019-3](https://doi.org/10.1016/0749-6419(89)90019-3)
39. Kumar M (2015) Dynamic characterization of the tool holder material: an experimental thesis Student thesis, KTH Royal Institute of Technology
40. Zhang SH, Zhang HY, Cheng M (2011) Tensile deformation and fracture characteristics of delta-processed Inconel 718 alloy at elevated temperatures. *Mater Sci Eng A* 528(19–20):6253–6258. <https://doi.org/10.1016/j.msea.2011.04.074>
41. Fisk M, Andersson J, du Rietz R, Haas S, Hall S (2014) Precipitate evolution in the early stages of ageing in Inconel 718 investigated using small-angle x-ray scattering. *Mater Sci Eng A* 612:202–207. <https://doi.org/10.1016/j.msea.2014.06.036>
42. Max B, Viguier B, Andrieu E, Cloue JM (2014) A re-examination of the Portevin-Le Chatelier effect in alloy 718 in connection with oxidation-assisted intergranular cracking. *Metall Mater Trans A* 45(12):5431–5441. <https://doi.org/10.1007/s11661-014-2508-6>
43. Chen W, Chaturvedi MC (1997) On the mechanism of serrated deformation in aged Inconel 718. *Mater Sci Eng A* 229(1–2):163–168. [https://doi.org/10.1016/S0921-5093\(97\)00005-1](https://doi.org/10.1016/S0921-5093(97)00005-1)
44. Zhou Z, Bhamare S, Ramakrishnan G, Mannava S, Langer K, Wen Y, Qian D, Vasudevan V (2012) Thermal relaxation of residual stress in laser shock peened Ti-6Al-4V alloy. *Surf Coat Technol* 206(22):4619–4627. <https://doi.org/10.1016/j.surfcoat.2012.05.022>

**Publisher's note** Springer Nature remains neutral with regard to jurisdictional claims in published maps and institutional affiliations.